nature communications

Article

https://doi.org/10.1038/s41467-025-68231-0

Thermotropic liquid-assisted interface management enables efficient and stable perovskite solar cells and modules

Received: 27 July 2025

Accepted: 23 December 2025

Published online: 07 January 2026

Check for updates

Qing Chang[1,2,5], Ruihao Chen[3,5,6] ✉, Yang Yang[3], Haosong Huang[2], Xiao Han[1,2], Xiaofeng Huang[2], Zhiyuan Dai[3], Binghui Wu[1], Jun Yin[1,2,4,6] ✉, Jing Li[1,2,4,6] ✉ & Nanfeng Zheng[2]

Despite substantial improvements in the quality of perovskite films achieved through processing optimization, the prevalence of surface and interfacial defects underscores the critical need for efficient post-treatment strategies. Here, we report an expectable surface engineering approach using thermotropic liquid molecule 1-boc-piperazine (1-BP). The 1-BP undergoes a solid-to-liquid phase transition and spontaneously migrates to perovskite grain boundaries during annealing process, forming an active encapsulation layer that reconstructs the perovskite interface. The most attractive achievement of ion migration suppression by 1-BP has been evidentially revealed by the in-situ time-of-flight secondary ion mass spectrometry. Base on the approach, the n-i-p perovskite solar cells achieve a certified power conversion efficiency of 25.62%, with perovskite solar modules achieving PCE of 22.03% (active area: 22.8 cm^2). Furthermore, the 1-BP engineered devices demonstrated exceptional stability, retaining T_{90} after 1500 h at 65 °C with continuous illumination and T_{87} after 1000 h at 85 °C/85% RH.

The metal halide perovskites show higher defect tolerance than other polycrystalline photovoltaic materials[1,2]. However, the perovskite/transport layers and grain boundaries (GBs) typically generate numerous unsaturated dangling bonds and vacancies[3], which further facilitate defect accumulation[4,5], ultimately forming carrier recombination centers that significantly compromise device performance[6,7]. Precisely designed low-dimensional architectures[8,9] and molecule regulator[10,11] can create passivation layers to suppress surface defects and block ion migration, managing this without hindering charge transport properties remains a major challenge for solid-state processing approaches[12].

Previous studies on interface defect management have primarily focused on interface engineering strategies under static conditions, where solid molecules remain anchored at their original positions after surface treatment[13,14]. These approaches exhibit significant limitations in maintaining stable interfacial modification effects under dynamic environments, making real-time repair of damaged interfaces challenging during post-annealing processes or operational conditions. This challenge is further exacerbated by the complex ion migration phenomena, which critically impact the long-term interface stability and device performance. Despite progress, substantial gaps remain in fully elucidating ion migrations pathways and in developing effective strategies to mitigate their detrimental effects[15].

In this study, we propose a dynamic passivation strategy that leverages interface management with coordinative and thermotropic liquid-crystal molecule, 1-Boc-piperazine (1-BP). This approach

[1]Pen-Tung Sah Institute of Micro-Nano Science and Technology, Xiamen University, Xiamen, China. [2]Innovation Laboratory for Sciences and Technologies of Energy Materials of Fujian Province, Xiamen, China. [3]School of Materials Science and Engineering, State Key Laboratory of Solidification Processing, Center for Nano Energy Materials, Northwestern Polytechnical University, Xi'an, China. [4]Engineering Research Center of Micro-nano Optoelectronic Materials and Devices, Ministry of Education, Xiamen University, Xiamen, China. [5]These authors contributed equally: Qing Chang, Ruihao Chen. [6]These authors jointly supervised this work: Ruihao Chen, Jun Yin, Jing Li. ✉e-mail: rhchen@nwpu.edu.cn; jyin@xmu.edu.cn; lijing@xmu.edu.cn

promotes the spontaneous migration and selective enrichment of 1-BP molecules at defect-prone GBs through post-treatment, creating a highly refined and reconstructed passivation layer due to its unique combination of coordinative properties and thermal fluidity. Furthermore, the in-situ TOF-SIMS test directly reveals the effective suppression of ion migration by 1-BP. Ultimately, this strategy increases the PCE of perovskite solar cells (PSCs) from 22.74% to 25.91% (a certified PCE of 25.62%). And the perovskite solar modules (PSMs) with active area of 22.8 cm^2 achieved an impressive PCE of 22.03%. Additionally, the optimized device maintains over 90% of its initial efficiency after 1500 h under ISOS-L-2 protocols.

Results

Elucidation of interface modification mechanisms

The thermal fluidity of 1-Boc-piperazine (1-BP) is evident from its solid-to-liquid phase transition at 50 °C, as depicted in Supplementary Fig. 1, in agreement with the differential scanning calorimetry (DSC) results in Supplementary Fig. 2. In addition, polarizing optical microscopy (POM) images in Supplementary Fig. 3 clearly confirm the solid-to-liquid transition of 1-BP upon heating. The proposed mechanism of 1-BP action with perovskites is illustrated in Fig. 1a. The thermotropic liquid nature of 1-BP enables homogeneous surface coverage while its excess molecules migrate to grain boundaries through thermal-induced fluidity. The molecular structure and electrostatic potential distribution of the 1-BP reveal its potential for interfacial modification (Fig. 1b). Theoretical analysis demonstrates that 1-BP can coordinatively passivate undercoordinated Pb^{2+} sites and halogen vacancies in perovskite, respectively, achieving synergistic defect passivation. Building on this molecular characteristic, the mechanism of suppressing iodide migration in perovskite systems was examined through first-principles calculations. The (010) surface of $FAPbI_3$ with an iodine vacancy (denoted as $FAPbI_3$(010)-Iv) was constructed to examine iodine migration (Fig. 1c). Slab model of $FAPbI_3$(010)-mol was built by constructing $FAPbI_3$(010) with 1-BP adsorbed on surface in Fig. 1d. As revealed by Supplementary Fig. 4 and Supplementary Table 1, the energy barriers for iodine migration in the pristine system were determined to be 0.33 eV for forward migration (into the vacancy) and 0.37 eV for reverse migration (out of the vacancy). Following 1-BP adsorption in the $FAPbI_3$(010)-Iv-mol system, it was observed that substantial structural reorganization occurs during iodine migration, characterized by coordinated movements of multiple atoms. The modified energy barriers of 0.17 eV (forward) and 0.47 eV (reverse) demonstrate enhanced iodine incorporation into vacancies while effectively suppressing iodine escape. This asymmetric energy landscape, with significantly reduced forward barrier and increased reverse barrier, suggests that 1-BP modification stabilizes the Pb-I inorganic framework through two mechanisms: (1) facilitating vacancy filling and (2) inhibiting iodine vacancy formation[16]. Consequently, the structural stability of perovskite films would be enhanced.

In addition, owing to this interaction, 1-BP anchored on the surface of the perovskite film also exhibits enhanced thermal stability relative to its bulk form, as confirmed by thermogravimetric analysis (TGA) (Fig. 1e). Specifically, neat 1-BP shows relatively low intrinsic thermal stability with an initial decomposition temperature of 143 °C. Upon adsorption onto the perovskite surface, a pronounced stabilization is observed: the decomposition temperature of 1-BP increases to 169 °C in Stage I, attributed to strong chemical bonding between 1-BP and the perovskite framework. Stage II, commencing at approximately 350 °C, corresponds to decomposition of the perovskite lattice itself, consistent with the TGA of the control perovskite film (326 °C, Supplementary Fig. 5).

To assess the surface topography of the modified perovskite film, scanning electron microscope (SEM) and atomic force microscopy (AFM) were conducted (Supplementary Fig. 6 and Supplementary Fig. 7). It can be observed that after 1-BP modification, the perovskite surface shows clear reconstruction, its surface becomes smoother, and the root-mean-square (RMS) roughness decreases from 23.33 nm to 16.29 nm. This improvement is attributed to the modification effect of thermotropic liquid molecules on the perovskite surface. The surface coating feature of 1-BP perovskite films were analyzed using AFM-based infrared spectroscopy (AFM-IR)[17,18]. By characterizing the infrared absorption of the unique amide group of 1-BP molecules at 1680 cm^{-1} and leveraging the spatial resolution of AFM, it was confirmed that the 1-BP molecules predominantly accumulated at the GBs due to thermal-induced flow (Fig. 1f, g). The averaged IR intensity distribution (Supplementary Fig. 8) at the characteristic wavenumber (1680 cm^{-1}) clearly confirms the presence of 1-BP molecules on the perovskite surface, whereas the control sample exhibits only background-level signal[18]. These results indicate that during thermal annealing, in addition to passivating the perovskite surface, excess 1-BP molecules spontaneously migrate to GBs driven by their thermotropic liquid properties.

As shown in Fig. 1h and Supplementary Fig. 9, high-resolution transmission electron microscopy (HR-TEM) images clearly reveal well-defined grain and grain boundary structures in the perovskite film[19], along with selective aggregation of excess 1-BP molecules at the GBs. Importantly, these results confirm that 1-BP dose not incorporate into the perovskite lattice[20]. To visualize the dynamic fluidity of excess 1-BP on the perovskite, a partially 1-BP coated perovskite film was monitored under thermal treatment using optical microscopy (Supplementary Fig. 10). Under continuous heating at 50 °C, thicker excess 1-BP aggregates gradually diffused into surrounding regions, whereas the pre-modified perovskite surface region showed negligible change. This demonstrates the thermotropic liquid behavior of excess 1-BP and the excellent thermal stability of the coordinated surface layer. This distinctive spatial distribution arises from the unique phase transition behavior of 1-BP under thermal conditions[21,22] and its specific interaction with the perovskite.

To further investigate the crystallinity changes in perovskite films induced by 1-BP, pole figure measurements were conducted along the (100) facet orientation (Supplementary Fig. 11)[23]. The diffraction signal exhibits enhanced crystallinity for the 1-BP-modified film with a stronger (100) facet orientation, accompanied by a notable reduction in miscellaneous peaks within 15°[24,25]. The surface reconstruction and enhanced crystal orientation for perovskite film by 1-BP was further verified in grazing-incidence wide-angle X-ray scattering (GIWAXS) vector in the specular direction ($\mathbf{q}_z$) of 1.0 $Å^{-1}$, as shown in Fig. 1i, j[26,27]. The results are consistent with the surface SEM images (Supplementary Fig. 6) and the cross-sectional SEM images in Supplementary Fig. 12, which reveal pronounced surface reconstruction and defect passivation with smoother and purer perovskite top surface morphology[28,29]. Based on the above crystallization analysis, it can be concluded that during the post-treatment process, the mild etching of IPA[30] at the perovskite surface together with strong chemical interactions between 1-BP and the perovskite, enables an effective surface reconstruction and interfacial management for the perovskite films. As a result, both surface crystallinity and the uniformity of grain orientation for perovskite films are simultaneously improved.

Chemical passivation and ion migration suppression

The interaction between 1-BP and perovskite was verified by Fourier transform infrared spectroscopy (FTIR) spectroscopy (Supplementary Fig. 13), evidenced by clear shifts in the -N-H and -C=O vibrational bands of 1-BP. The detailed chemical interaction between 1-BP with perovskites and associated passivation effect were further investigated by X-ray photoelectron spectroscopy (XPS) and photoluminescence (PL) spectra. After the surface modification of the perovskite with 1-BP, the main peaks at 144.10 eV (Pb $4f_{5/2}$) and 139.23 eV (Pb $4f_{7/2}$) shifted to lower binding energy regions (143.39 eV and 138.52 eV, respectively) (Supplementary Fig. 14)[31]. Additionally, compared to the control film,

https://doi.org/10.1038/s41467-025-68231-0

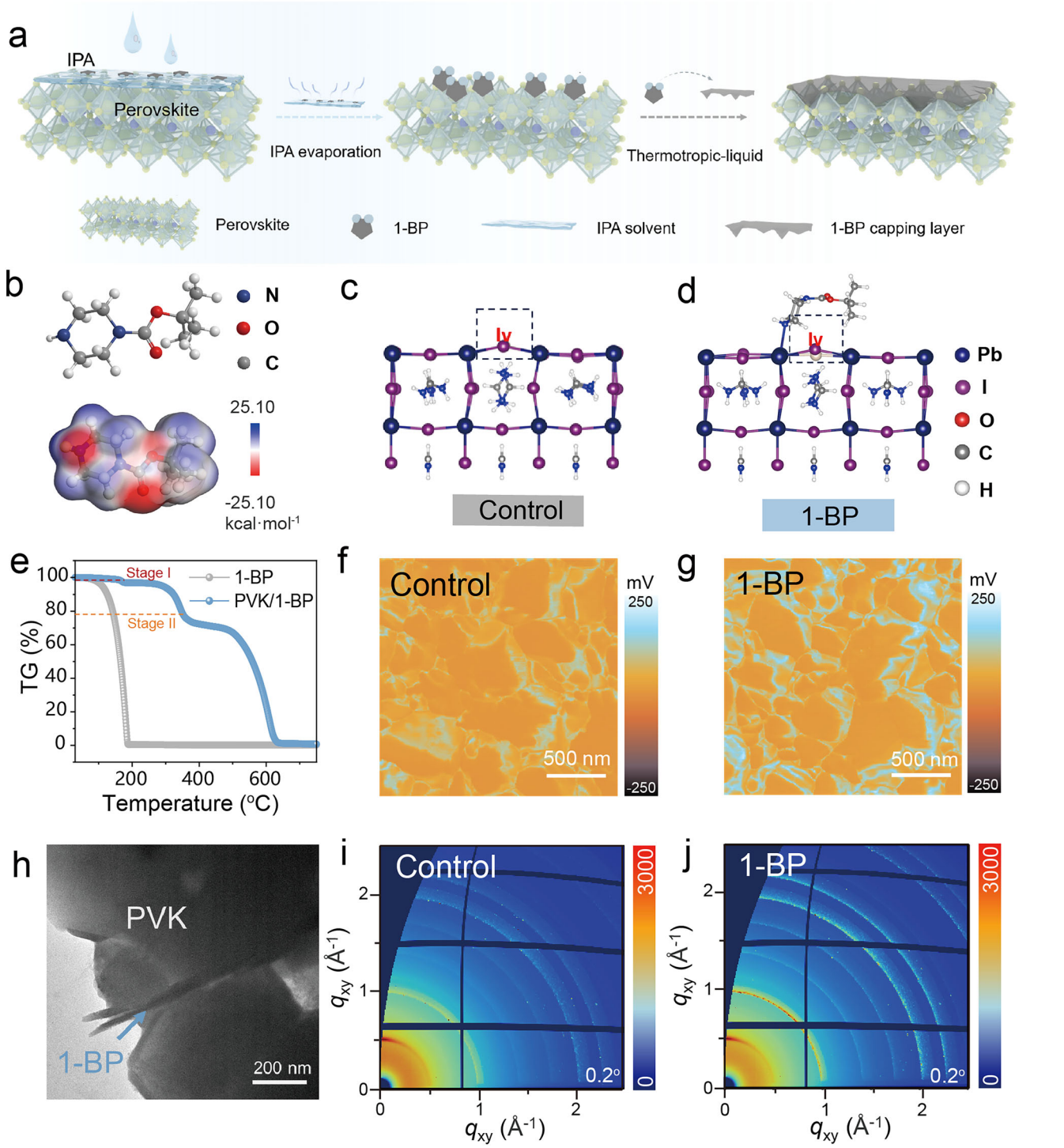

Fig. 1 | Thermotropic properties of 1-BP and their influence on perovskite films management. a Schematic of 1-BP and conventional passivation methods modified perovskite films. **b** The molecular structures and electrostatic potentials of 1-BP. The color bar from blue to red marks the increment of EPR. Schematic of (**c**) control and (**d**) 1-BP modification perovskite interface for I vacancy. **e** Synchronous thermogravimetric analysis (TGA) detection for 1-BP and perovskite/1-BP. AFM-IR topographic and corresponding 1680 cm^{-1} absorption images on top surface of (**f**) control and (**g**) 1-BP films. The High-resolution transmission electron microscopy (HR-TEM) image of the (**h**) 1-BP perovskite. 2D GIWAXS data of the (**i**) control and (**j**) 1-BP perovskite films.

the metal Pb peaks near the main peaks in the 1-BP perovskite film disappeared. The results well indicate the interaction between the 1-BP molecules and uncoordinated Pb ions[32]. The main peaks at 631.64 eV (I $3d_{5/2}$) and 620.15 eV (I $3d_{3/2}$) also shifted to lower binding energy regions (630.92 eV and 619.42 eV, respectively), indicating the interaction between I-1-BP and the perovskite film[33]. The PL spectra in Supplementary Fig. 15 shows enhanced the intensity from the 1-BP modified film due to the passivation effect, and the reconstructed perovskite film exhibits an increased excited state lifetime (Supplementary Table 2). This observation is consistent with the increased formation energy of iodine vacancy.

Given the surface reconstructive effect and chemical bonding of 1-BP on perovskite films, the stability of the 1-BP modified films was subsequently investigated. The in-situ ToF-SIMS was employed to

https://doi.org/10.1038/s41467-025-68231-0

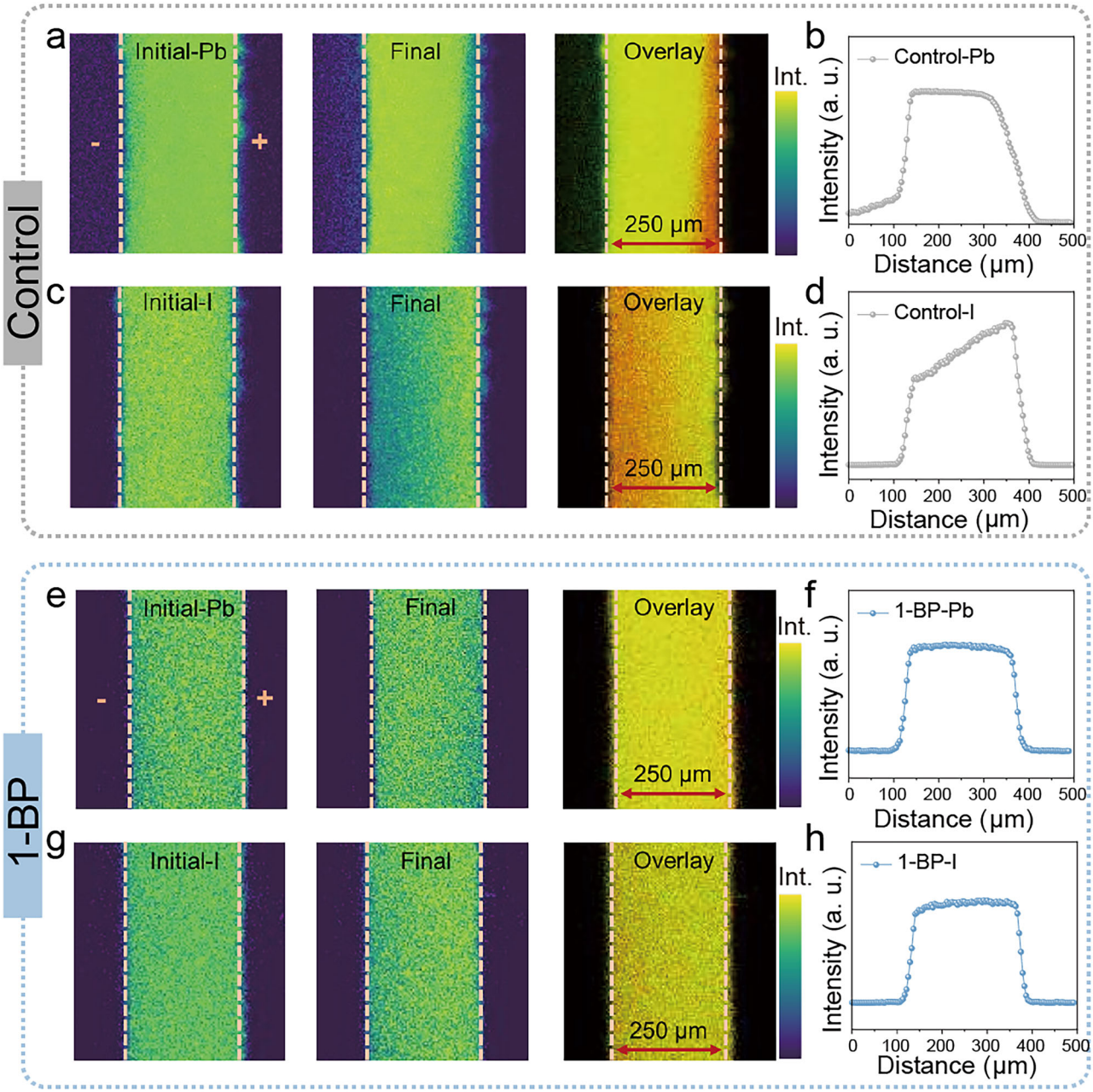

Fig. 2 | The in-situ ToF-SIMS investigation of ion migration in perovskites under applied electric field. Pb-ion distribution of perovskite film surface in (**a**, **b**) control and (**e**, **f**) 1-BP perovskite films; I-ion distribution of perovskite film surface in (**c**, **d**) control and (**g**, **h**) 1-BP perovskite films.

reveal the spatial distribution of chemical components at the molecule level, monitoring and evaluating the ion migrations in the perovskite under an electric field in real-time[34]. A schematic diagram of the experimental setup is presented in Supplementary Fig. 16. To avoid chemical contamination from the top electrode and surface contaminants in vertically structured devices, we used a lateral device structure and sputtered away surface contaminants with an Ar ion gun before the experiments.

As the applied electric field (stabilized at each field strength for 120 s) gradually increased, both Pb^{2+} and I^- exhibit significant migration under the electric field for the control sample, with noticeable accumulation observed at the electrodes (Fig. 2a, c)[35]. The integral scan profiles of the initial and final states for the control film (Fig. 2b, d) also show the similar results. In contrast, the 1-BP-modified film (Fig. 2e, g) exhibits no significant changes before and after the application of the electric field. The integral scan profiles (Fig. 2f, h) more clearly demonstrate the effective suppression of I^- and Pb^{2+} migration and diffusion by 1-BP[36]. The results were consistent with the TOF-SIMIS spectra of the device in the vertical direction (Supplementary Fig. 17). The distribution of Pb^{2+} and I^- ions in perovskite devices fabricated with 1-BP-modified films shows distinct trends after aging at 85 °C under illumination for 100 h. While in the control device (Supplementary Fig. 17a–c), Pb^{2+} ions exhibit upward diffusion, and the reaction between the metal electrode and halides is more pronounced, where Au demonstrates significant ion migration and diffusion within the perovskite layer. In contrast, the 1-BP-treated device (Supplementary Fig. 17d–f) effectively suppresses the downward migration of metal ions.

Device performance based on 1-BP engineering

The photovoltaic devices adopting an n-i-p architecture (as illustrated in Fig. 3a) were subsequently manufactured and characterized under standard test conditions (100 mW cm^{-2}, AM 1.5 G spectrum). The

https://doi.org/10.1038/s41467-025-68231-0

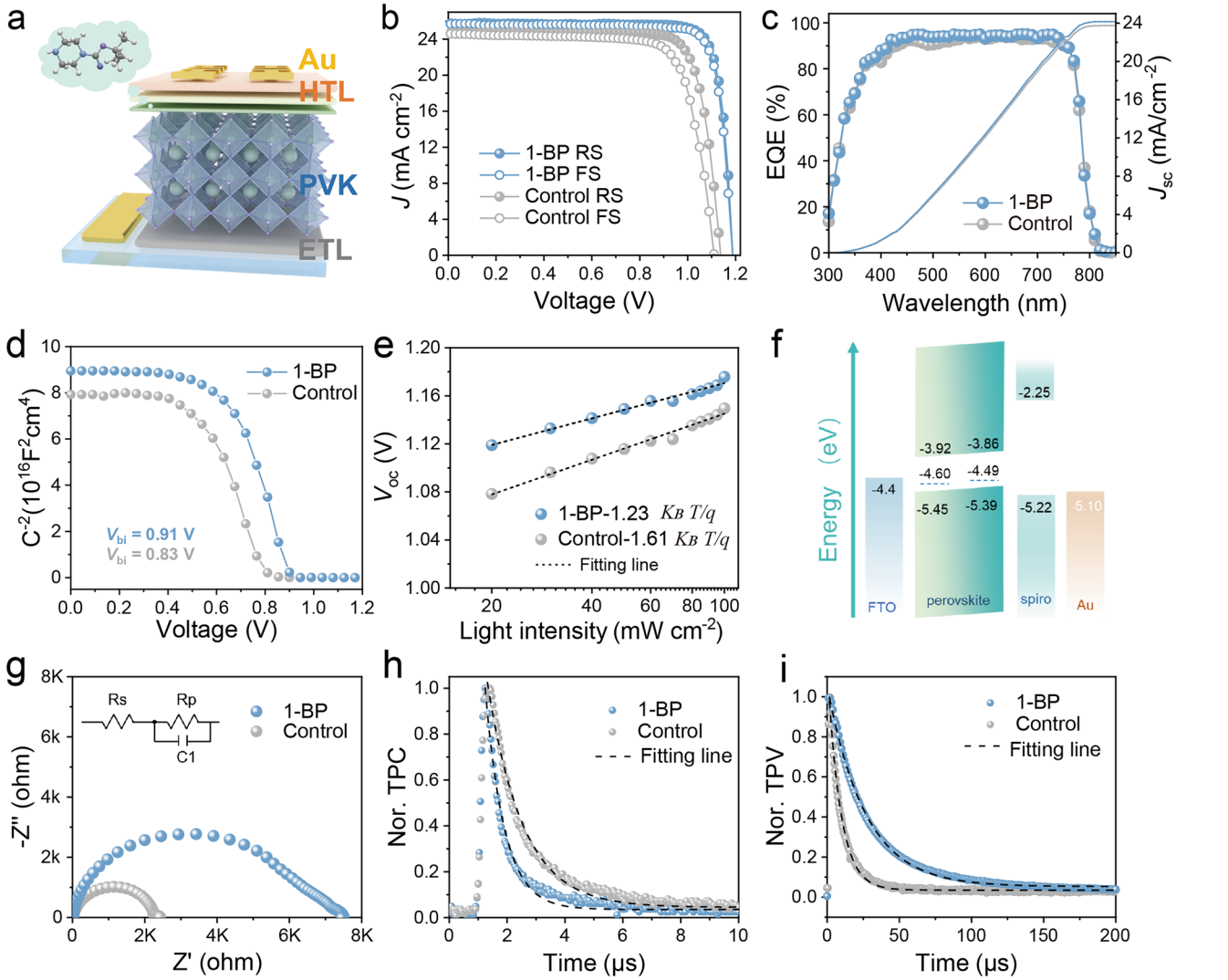

Fig. 3 | Photovoltaic performance of 1-BP engineered devices. a Schematic of 1-BP modified PSC structure. **b** *J*–*V* curves of the best-efficiency control and 1-BP devices. **c** EQE spectra with the integrated J_{sc}. **d** Mott-Schottky plots and (**e**) Dependence of V_{oc} at various light intensities for the control and 1-BP devices. **f** The schematic diagram of energy levels. **g** Nyquist plots of the Control and 1-BP PSCs under dark condition. **h** TPC and **i** TPV decay curves of the control and 1-BP PSCs.

photovoltaic performance of 1-BP devices with different concentrations (0.01, 0.05 and 0.1 mg mL^{-1}) surpasses that of control samples (Supplementary Fig. 18), with their champion PCE *J*-*V* curves displayed in Supplementary Fig. 19. The detailed photovoltaic parameters were summarized in Supplementary Table 3. The control device had a maximum PCE of 22.74% with a V_{oc} of 1.14 V and a fill factor of 80.99%. While the champion 1-BP of 0.05 mg mL^{-1} PSC showed an excellent maximum PCE of 25.91% with a V_{oc} of 1.18 V and a fill factor of 84.51% (Fig. 3b). Furthermore, PL measurements (Supplementary Fig. 20) show that perovskite films treated with 0.05 mg mL^{-1} 1-BP exhibit stronger PL intensity than those treated with 0.01 and 0.10 mg mL^{-1}. XRD results (Supplementary Fig. 21) also confirm that the 0.05 mg mL^{-1} 1-BP treatment leads to enhanced crystallinity and a reduced PbI_2 peak intensity, indicating optimal passivation at this concentration. The independently certified PCE results (Supplementary Fig. 22) demonstrate that the 1-BP-PSCs achieved a champion efficiency of 25.62%. The integrated short-circuit current densities deduced from the incident photo-to-electron conversion efficiency (IPCE) spectra in Fig. 3c are 23.74 mA cm^{-2} and 24.16 mA cm^{-2} for the reference and 1-BP-modified devices, respectively, showing good agreement with the J_{sc} values obtained from solar simulator measurements.

Owing to the improved energy alignment, the built-in potential (V_{bi}) has been obviously improved, as demonstrated by the Mott-Schottky analysis (Fig. 3d). The V_{bi} of 1-BP was measured to be 0.91 V, in comparison with that of 0.83 V for the control sample. Additionally, the V_{oc} dependence curve of 1-BP PSCs exhibits a shallower slope (Fig. 3e), which further corroborates the observed increases in V_{oc} and FF in the 1-BP devices[37]. To further understand the improvement in PSC performance due to interfacial management, the improved energy levels alignment of perovskite induced by 1-BP was evaluated by ultraviolet photoelectron spectroscopy (UPS) measurements. The work function (W_F) values have been found to be rise from 4.60 to 4.49 eV after the 1-BP modified (Supplementary Fig. 23), and the valence band maximums (V_{BM}) were declined below Fermi levels (E_F) by 0.87 and 0.90 eV, respectively. The results are consistent with the subsequent Kelvin probe force microscopy (KPFM) test[38]. As shown in Supplementary Fig. 24, the uniformly increased potential difference between the film and the probe indicates a higher WF after 1-BP modification. Accordingly, the energy level diagram can be illustrated as in Fig. 3f, showing that the 1-BP film exhibits relative stronger p-type property on the perovskite surface, which facilitates improved charge transport.

Electrochemical impedance spectroscopy analysis revealed reduced charge-transfer resistance and enhanced recombination resistance (Fig. 3g and Supplementary Table 4), demonstrating more efficient charge extraction and suppressed recombination losses. These findings were corroborated by transient optoelectronic measurements, where both photocurrent decay (TPC) and photovoltage decay (TPV) analyses confirmed accelerated charge extraction kinetics and diminished recombination pathways in the 1-BP-modified devices[39]. As shown in Fig. 3h, i, the TPC decay rate of the 1-BP device is faster, while the TPV decay rate is slower (Supplementary Table 5) comparing with the control sample[40]. Notably, the substantially lower dark leakage current observed in 1-BP devices (Supplementary Fig. 25) provides additional evidence for its superior charge-carrier management.

Solar module performance and stability

Furthermore, we systematically evaluated the optoelectronic properties of the modified perovskite films and their corresponding interfaces in 6×6 cm^2 perovskite solar modules. Figure 4a illustrates the encapsulated structure of the module, which was designed based on the thermotropic liquid properties of 1-BP. The champion PCE of reverse scan (RS) 22.03% (forward scan, FS 20.83%) was achieved, while the control PSMs displayed lower efficiencies of RS 19.91% and FS 18.01% with areas of 36 cm^2 (active area 22.8 cm^2) (Fig. 4b), and specific parameters are detailed in Supplementary Table 6.

The improved stability for the perovskite films was also evaluated under accelerated aging at 85 °C by the in-situ PL spectra (Fig. 4c, d). Under 375 nm laser (0.3 W) in N_2 box, the fluorescence intensity of the control sample deteriorated rapidly within 20 min, whereas the 1-BP modified sample maintained an excellent stable fluorescence intensity. The improved thermal stability is attributed to strengthened interfacial bonding, effective vacancy suppression, and stabilized Pb-I bonds via 1-BP passivation. Also, the thermally driven mobility of 1-BP further allows rapid passivation of heat or laser-induced defects, preserving stable optoelectronic performance. Supplementary Fig. 26 presents PL mapping images of the control and 1-BP perovskite films in both fresh and aged states. The fresh 1-BP film (0 h) exhibits stronger and more uniform PL intensity compared to the control, indicating improved crystallinity and film quality due to effective passivation by 1-BP. After aging for 100 h at 65 °C and 60 ± 10% relative humidity (RH), the control film develops pronounced dark spots, which can be attributed to defect aggregation at grain boundaries. In contrast, the 1-BP film maintains homogeneous luminescence, demonstrating its superior stability under harsh environmental conditions. Moreover, the water contact angle of the perovskite film increases from 47° to 61° after 1-BP modification (Supplementary Fig. 27), corroborating the enhanced moisture stability.

The PSCs were then subjected to a simulated natural diurnal cycle to assess the long-term stability under light-dark conditions, with a cycle of 10 h of light followed by 10 h of darkness, and the results are shown in Fig. 4e, f. Compared to the control sample, which exhibited a

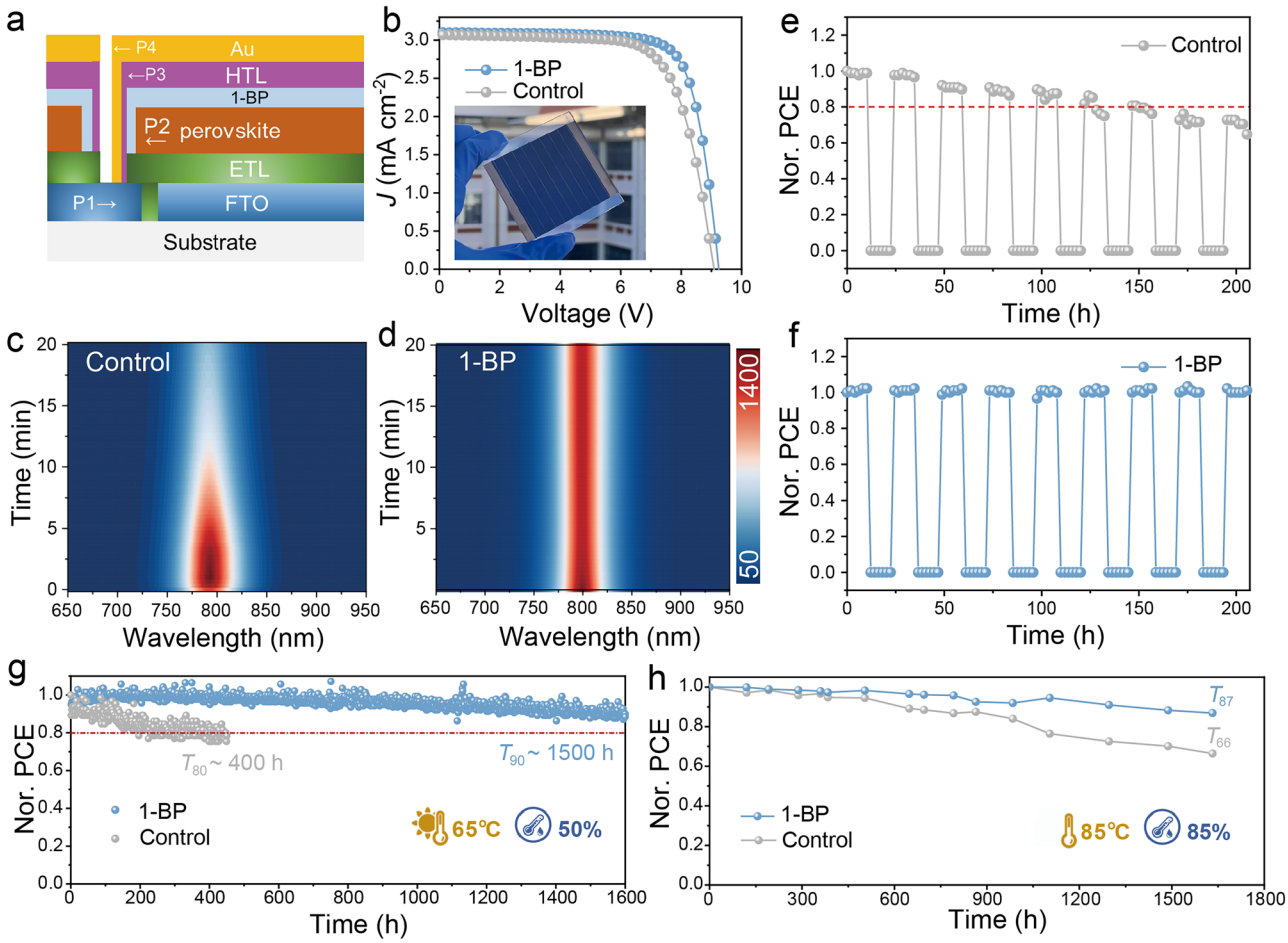

Fig. 4 | Photovoltaic performance and stability of solar modules. a Schematic illustration of the module's configuration. **b** *J–V* curves of the champion modules (6 × 6 cm^2) based on the 1-BP modified perovskite films The inset shows a photo of PSM device. In-situ PL spectra of (**c**) control and (**d**) 1-BP perovskite films aged at 85 °C under 375 nm laser in N_2 box. Light-dark cycle stability of **e** control and **f** 1-BP PSMs. **g** Operation stability of the control and 1-BP encapsulated PSMs at max power point tracking under AM 1.5 G illumination. **h** Thermal stability of the encapsulated control and 1-BP PSMs under 85 °C and 85% RH conditions.

significant decline after the third cycle (40 h) and dropped to 80% of its initial efficiency by 160 h, the 1-BP-treated device showed no notable degradation within 200 h, demonstrating superior light-dark cycle stability.

The long-term operational stability of encapsulated PSMs was evaluated under maximum power point tracking conditions (65 °C, ISOS-L-2), with the corresponding performance degradation profile presented in Fig. 4g. The control module maintained T_{80} stability within 400 h, whereas the 1-BP module exhibited T_{90} stability over an extended period of 1500 h. The corresponding photovoltaic parameters before and after aging are summarized in Supplementary Table 7. Furthermore, under the ISOS-D-3 protocol, the devices were encapsulated and subjected to a dark environment at 85 °C and 85% relative humidity, with continuous monitoring of their PCE. The results depicted in Fig. 4h reveal that, in contrast to the control sample (T_{66}), the 1-BP treated devices retained T_{87} stability even after 1500 h, and the photovoltaic performances of modules before and after aging test at ISOS-D-3 were summarized in Supplementary Table 8. These results demonstrated that 1-BP has significantly enhanced the stability of perovskite films and devices under conditions of light, heat, and electric field exposure. More broadly, this work establishes a general selection framework grounded in thermotropic liquid-assisted interface management. By choosing molecular candidates with tailored liquid-crystalline phase transition temperatures and functional groups, the strategy can be tuned to diverse environmental and operational conditions, thereby advancing the long-term stability of perovskite optoelectronic devices.

Discussion

In this work, we develop a thermotropic liquid-assisted interface management strategy for perovskite films, systematically investigating its active passivation mechanisms and crystallization regulation effects. Through in-situ TOF-SIMS technology, the passivation effect of 1-BP molecules was directly observed that significantly inhibits ion migration in perovskite. Based on this surface management strategy, the perovskite solar cells achieved a certified PCE of 25.62%, while perovskite solar modules prepared reached a PCE of 22.03% at active area of 22.8 cm^2. More importantly, the stability of solar modules under continuous illumination, light-dark cycling, and high-temperature conditions at 65 °C was significantly enhanced. This research not only provides a surface management paradigm for perovskite optoelectronics but also offers a viable pathway toward industrial-scale manufacturing.

Methods

Materials

Xi'an Polymer Light Technology Corp provided cesium iodide (CsI), lead chloride ($PbCl_2$), spiro-OMeTAD, PTAA, and FK-209 Co(III) TFSI salt; Advanced Election Technology Co., Ltd supplied lead iodide (PbI_2), formamidinium iodide (FAI), and 4-tert-butylpyridine (t-BP). Bis(trifluoromethane)sulfonimide lithium salt (Li-TFSI) was procured from both Alfa-Aesar and Sigma-Aldrich, while high-purity chlorobenzene (CB, 99.9%), osopropyl alcohol (IPA, 99.9%) and N-methylpyrrolidone (NMP, 99.5%) were obtained from Alfa Aesar.

Precursor preparation and devices fabrications

The entire fabrication process was carried out in a glove box filled with N_2, with the temperature controlled at 20 ± 5 °C. The SnO_2 electron transport layer was fabricated using chemical bath deposition (CBD). For the small area PSCs, the $FA_{0.97}Cs_{0.03}PbI_3$ perovskite films were synthesized using a precursor solution containing stoichiometric amounts of CsI (0.03 mmol), FAI (0.97 mmol), and PbI_2 (1.00 mmol) dissolved in 600 μL dimethylformamide (DMF). To enhance crystallization, methylammonium chloride (MACl, 20 mg) and N-methyl-2-pyrrolidone (NMP, 96 μL) were incorporated as additives. The precursor solution was spin-coated onto CBD-SnO_2 substrates at 6000 rpm for 30 s. At 27 s into spinning, 120 μL ethyl acetate was dripped onto the wet film as an antisolvent. The resulting films were then thermally annealed in N_2 atmosphere using a two-step process: first at 110 °C for 30 min, followed by 130 °C for another 30 min. For the PSMs, the perovskite material employed in this study was $FA_{0.95}Cs_{0.05}PbI_3$, and the perovskite film was prepared using a combination of blade-coating and vacuum-flash techniques. The substrate with an area of 36 cm^2 was placed under the blade with adjusted height. The initial speed of the blade coating was set to 1.6 mm s^{-1}. The first segment of the coating process involved a constant speed over a distance of 20 mm, while the second segment involved a variable speed over a distance of 40 mm, with an acceleration rate of 0.05 mm s^{-1}. After the blade coating process, the substrate was immediately transferred to the vacuum flash chamber. The vacuum-flash process was completed when the chamber pressure was dropped to 10 Pa from the atmospheric pressure within 10 s. Then, the substrate was quickly transferred to the hot plant, of which the output temperature was set at 150 °C with a treatment duration of 30 min. The 1-BP molecules were dissolved in isopropanol at concentrations of 0.01, 0.05, and 0.10 mg mL^{-1}, respectively. These solutions were subsequently deposited onto the surface of the perovskite films, followed by annealing at 100 °C for 5 min. The hole-transport layer was fabricated using a solution-processed Spiro-OMeTAD formulation, consisting of 90 mg Spiro-OMeTAD dissolved in 1 mL chlorobenzene with 4.0 mol% Li-TFSI (in acetonitrile) and 20 μL 4-tert-butylpyridine (t-BP) additives. For the back electrode, an 80-nm-thick Au layer was thermally evaporated under vacuum conditions. Regarding the module fabrication, laser patterning (P2 and P3 processes) was performed using a computer-controlled laser scribing system to establish series interconnections between adjacent sub-cells. Module encapsulation: First, laser scribing was employed to remove the excess edges of every large-area perovskite film. Then, a polyisobutylene sealant and protective glass were layered onto every module. After preparation, the device was placed in a vacuum laminator to bond the module with the cover glass. The lamination process-maintained 90 °C for 10 min.

Theoretical calculations

All density functional theory (DFT) calculations were performed using the Vienna Ab-initio Simulation Package (VASP) with the projector augmented wave (PAW) method, employing the Perdew-Burke-Ernzerhof (PBE) functional combined with DFT-D3 dispersion correction and a plane-wave cutoff energy of 450 eV. Structural optimizations utilized different Monkhorst-Pack *k*-point meshes: 4 × 4 × 4 for $FAPbI_3$ bulk lattice optimization, 9 × 6 × 3 for I_2 bulk structure optimization, and 1 × 2 × 1 for $FAPbI_3$(010) surface and slab models, where the bottom half of atoms were fixed during relaxation. The calculations employed a self-consistent convergence threshold of 10^{-5} eV and geometry optimization criteria of maximum atomic forces below 0.02 eV $Å^{-1}$, with spin-polarization included to properly account for magnetic effects in the slab models.

Adsorption energy of 1-Boc-piperazine was determined by E_{ads}. $E_{ads} = E(AB) - E(A) - E(B)$. E(AB) represents the total energy of $FAPbI_3$(010) or $FAPbI_3$(010)-Iv with 1-Boc-piperazine adsorbed on surface. $E(A)$ represent the total energy of clean surface of $FAPbI_3$(010) or $FAPbI_3$(010)-Iv. $E(B)$ represent the total energy of 1-Boc-piperazine in its gas phase. Configuration of 1-Boc-piperazine was optimized in a 20 × 20 × 20 $Å^3$ cell box.

Formation energy of I vacancy was determined by E_f. $E_f = E(C) - E(D) - 0.5E(I_2\text{-bulk})$. $E(C)$ represents the total energy of $FAPbI_3$(010)-Iv or $FAPbI_3$(010)-Iv-mol. $E(D)$ represents the total energy of $FAPbI_3$(010) or $FAPbI_3$(010)-mol. The total energy of I atom equals to half of the total energy of I_2 bulk structure.

Immigration path of I atom in $FAPbI_3$(010)-Iv and $FAPbI_3$(010)-Iv-mol was searched by the Climbing Image Nudged Elastic Band (CINEB) method. In CINEB method, energy criterion and stress criterion were set at 10^{-7} eV and 0.05 eV $Å^{-1}$, respectively.

Characterization

The structural and optoelectronic properties were characterized using complementary analytical techniques: X-ray diffraction (XRD) analysis was conducted on a Thermo Scientific ARL EQUINOX 3500 diffractometer with Cu Kα radiation ($\lambda = 1.5406$ Å).

The spectral response was evaluated through External Quantum Efficiency (EQE) measurements performed using an Enlitech QE-R system equipped with a calibrated silicon reference cell.

The thermal stability of samples was measured by a HITACHI STA200 simultaneous thermogravimetric analyzer with a heating rate of 10 °C min^{-1} from room temperature to 800 °C at N_2 atmosphere.

Atomic force microscopy-infrared spectroscopy (AFM-IR) measurements were conducted on a Bruker nano-IR3 system.

High-resolution transmission electron microscopy (HRTEM) was conducted using a FEI Tecnai F30 transmission electron microscope, combined with an Oxford Instruments energy dispersive spectrometer and HAADF STEM detector, at an accelerating voltage of 300 kV. For 1-BP treatment, the perovskite polycrystalline films were immersed in a 1-BP solution to achieve complete surface coverage.

Surface morphology was examined using a Zeiss GeminiSEM500 field-emission SEM.

The crystalline properties of perovskites were characterized by XRD (Bruker D8 ADVANCE), with additional pole figure analysis.

The polarized optical microscopy (POM) observations were performed using a CX40P microscope (NINGBO SUNNY OPOTECH CO., LTD) equipped with a Linkam THMS600 heating stage. Images were captured at temperatures of 30 °C, 50 °C, 70 °C, and 90 °C.

The grazing-incidence wide-angle X-ray scattering (GIWAXS) measurements were performed at BL02U2 beamline of the Shanghai Synchrotron Radiation Facility (SSRF).

TOF-SIMS profiling was performed on an IONTOF-M6 system to study ion migration in FTO/Perovskite(/1-BP)/Au devices under 0–18 V bias. The overlay result represents the superposition of the initial and final states of Pb and I signal concentrations in the perovskite film before and after ion migration. The linear profiles were obtained by integrating the Pb and I signal intensities across the entire channel.

Optical properties were assessed through PL mapping (Nanophoton RAMAN-11) and TRPL measurements (Edinburgh Instruments FLS1000).

Current-voltage (J–V) characteristics of the devices were measured using a Keithley 2400 source measure unit equipped with a Class AAA solar simulator (450 W xenonlamp, Newport 94023 A).

The device stability was systematically evaluated under multiple stress conditions using specialized testing platforms. Continuous operational stability was monitored through maximum power point (MPP) tracking at 65 °C in ambient air, incorporating simulated diurnal cycling to evaluate light-dark transition effects (Multi-Channels Solar Cells Stability Test System, Wuhan 91PVKSolar Technology).

The accelerated degradation assessment was performed under 85 °C/85% RH conditions using a climate-controlled reliability chamber (K3600, McScience).

Reporting summary

Further information on research design is available in the Nature Portfolio Reporting Summary linked to this article.

Data availability

All data are available in the main text or the supplementary materials. Source data are provided with this paper.

References

1. Liu, G. et al. Dynamic defect tolerance in metal halide perovskites: from phenomena to mechanism. *Adv. Energy Mater.* **16**, 2405239 (2025).
2. Steirer, K. X. et al. Defect tolerance in methylammonium lead triiodide perovskite. *ACS Energy Lett.* **1**, 360–366 (2016).
3. Peng, J. et al. Interface passivation using ultrathin polymer–fullerene films for high-efficiency perovskite solar cells with negligible hysteresis. *Energy Environ. Sci.* **10**, 1792–1800 (2017).
4. Yang, S. et al. Stabilizing halide perovskite surfaces for solar cell operation with wide-bandgap lead oxysalts. *Science* **365**, 473–478 (2019).
5. Hu, M. et al. Post-treatment of metal halide perovskites: from morphology control, defect passivation to band alignment and construction of heterostructures. *Adv. Energy Mater.* **13**, 2301888 (2023).
6. Bisquert, J. Electrical charge coupling dominates the hysteresis effect of halide perovskite devices. *J. Phys. Chem. Lett.* **14**, 1014–1021 (2023).
7. Yin, L. et al. A multifunctional molecular bridging layer for high efficiency, hysteresis-free, and stable perovskite solar cells. *Adv. Energy Mater.* **13**, 2301161 (2023).
8. Yang, W. et al. Visualizing interfacial energy offset and defects in efficient 2D/3D heterojunction perovskite solar cells and modules. *Adv. Mater.* **35**, 2302071 (2023).
9. Jang, Y.-W. et al. Intact 2D/3D halide junction perovskite solar cells via solid-phase in-plane growth. *Nat. Energy* **6**, 63–71 (2021).
10. Kim, J. et al. Susceptible organic cations enable stable and efficient perovskite solar cells. *Joule* **9**, 101879 (2025).
11. Lee, J.-W., Tan, S., Seok, S. I., Yang, Y. & Park, N.-G. Rethinking the A cation in halide perovskites. *Science* **375**, eabj1186 (2022).
12. Teale, S., Degani, M., Chen, B., Sargent, E. H. & Grancini, G. Molecular cation and low-dimensional perovskite surface passivation in perovskite solar cells. *Nat. Energy* **9**, 779–792 (2024).
13. Wen, Y. et al. Rational design of molecular passivator to mitigate surface defects and stabilize organic cation in perovskite photovoltaics. *Adv. Energy Mater.* **15**, 2500389 (2025).
14. Liu, C. et al. Two-dimensional perovskitoids enhance stability in perovskite solar cells. *Nature* **633**, 359–364 (2024).
15. Yantara, N. & Mathews, N. Toolsets for assessing ionic migration in halide perovskites. *Joule* **8**, 1239–1273 (2024).
16. Liang, J., Lan, M. H., Pang, J., Xia, X. H. & Li, J. Nanometer-resolved mapping of organic cation migration behavior in methylammonium lead halide perovskites. *Angew. Chem. Int. Ed. Engl.* **63**, e202410557 (2024).
17. Lee, M. et al. Scanning probe microscopy of halide perovskite solar cells. *Adv. Mater.* **36**, 2407291 (2024).
18. Tan, Q. et al. Inverted perovskite solar cells using dimethylacridine-based dopants. *Nature* **620**, 545–551 (2023).
19. Sun, R. et al. A stepwise melting-polymerizing molecule for hydrophobic grain-scale encapsulated perovskite solar cell. *Adv. Mater.* **37**, 2410395 (2025).
20. Ma, Y. et al. Understanding microstructural development of perovskite crystallization for high performance solar cells. *Adv. Mater.* **35**, 2306947 (2023).
21. Du, X. et al. Spontaneous interface healing by a dynamic liquid-crystal transition for high-performance perovskite solar cells. *Adv. Mater.* **34**, 2207362 (2022).
22. Guo, Q. et al. Universal dynamic liquid interface for healing perovskite solar cells. *Adv. Mater.* **34**, 2202301 (2022).
23. Luo, C. et al. Facet orientation tailoring via 2D-seed- induced growth enables highly efficient and stable perovskite solar cells. *Joule* **6**, 240–257 (2022).

24. Li, X. et al. Bifunctional ligand-induced preferred crystal orientation enables highly efficient perovskite solar cells. *Joule* **8**, 3169–3185 (2024).
25. Ma, C. et al. Photovoltaically top-performing perovskite crystal facets. *Joule* **6**, 2626–2643 (2022).
26. Yang, Y. et al. Synchrotron radiation-based in situ giwaxs for metal halide perovskite solution spin-coating fabrication. *Adv. Sci.* **11**, 2403778 (2024).
27. Chen, Y. et al. Nuclei engineering for even halide distribution in stable perovskite/silicon tandem solar cells. *Science* **385**, 554–560 (2024).
28. Wang, S. et al. In situ self-elimination of defects via controlled perovskite crystallization dynamics for high-performance solar cells. *Adv. Mater.* **35**, 2305314 (2023).
29. Geng, C. et al. Crystallization modulation and holistic passivation enables efficient two-terminal perovskite/CuIn(Ga)Se_2 tandem solar cells. *Nano-Micro Lett.* **17**, 8 (2024).
30. Tan, S. et al. Surface reconstruction of halide perovskites during post-treatment. *J. Am. Chem. Soc.* **143**, 6781–6786 (2021).
31. Li, M. et al. Orientated crystallization of FA-based perovskite via hydrogen-bonded polymer network for efficient and stable solar cells. *Nat. Commun.* **14**, 573 (2023).
32. Chang, Q. et al. Ferrocene-induced perpetual recovery on all elemental defects in perovskite solar cells. *Angew. Chem. Int Ed. Engl.* **60**, 25567–25574 (2021).
33. Yang, Y. et al. Multifunctional molecule interface modification for high-performance inverted wide-bandgap perovskite cells and modules. *J. Mater. Chem. A* **11**, 16871–16877 (2023).
34. Higgins, K. et al. Exploration of electrochemical reactions at organic–inorganic halide perovskite interfaces via machine learning in in situ time-of-flight secondary ion mass spectrometry. *Adv. Funct. Mater.* **30**, 2001995 (2020).
35. Pospisil, J. et al. Reversible formation of gold halides in single-crystal hybrid-perovskite/Au interface upon biasing and effect on electronic carrier injection. *Adv. Funct. Mater.* **29**, 1900881 (2019).
36. Birkhold, S. T. et al. Interplay of mobile ions and injected carriers creates recombination centers in metal halide perovskites under bias. *ACS Energy Lett.* **3**, 1279–1286 (2018).
37. Yang, Y. et al. Bilateral chemical linking at NiOx buried interface enables efficient and stable inverted perovskite solar cells and modules. *Angew. Chem. Int. Ed. Engl.* **63**, e202409689 (2024).
38. Chen, R. et al. Conformal imidazolium 1D perovskite capping layer stabilized 3D perovskite films for efficient solar modules. *Adv. Sci.* **9**, 2204017 (2022).
39. Yang, T. et al. One-stone-for-two-birds strategy to attain beyond 25% perovskite solar cells. *Nat. Commun.* **14**, 839 (2023).
40. Luo, Y. et al. Dissolved-Cl2 triggered redox reaction enables high-performance perovskite solar cells. *Nat. Commun.* **14**, 3738 (2023).

Acknowledgements

R.C. acknowledges the National Natural Science Foundation of China (22375163, 52203338). Y.J. acknowledges the Science and Technology Programs of Fujian Province (2022H0005) and Fundamental Research Funds for the Central Universities (20720240067). J. L. acknowledges China Huaneng Group Key R&D Program (HNKJ22-H104) and Technology Projects of Innovation Laboratory for Sciences and Technologies of Energy Materials of Fujian Province (RD2022040601).

Author contributions

Q.C. and R.C. conceived the idea, Q.C. conducted the relevant measurements and fabricated all the devices. Y.Y., J.L. and J.Y. conceived the paper. H.H., Z.D. assisted to the stability measurements. X.H., X.H., B.W., and N.Z. coordinated the whole project. Q.C. wrote the manuscript. J.L., R.C. and J.Y. supervised this work.

Competing interests

The authors declare no competing interests.

Additional information

Supplementary information The online version contains supplementary material available at https://doi.org/10.1038/s41467-025-68231-0.

Correspondence and requests for materials should be addressed to Ruihao Chen, Jun Yin or Jing Li.

Peer review information *Nature Communications* thanks Ran Chen, Shengchun Qu, Yanlin Song and the other anonymous reviewer(s) for their contribution to the peer review of this work. A peer review file is available.